

What is heating the quiet-Sun chromosphere?

S. Wedemeyer-Böhm^{1,2}, O. Steiner¹, J. Bruls¹, and W. Rammacher¹

¹*Kiepenheuer-Institut für Sonnenphysik, Schöneckstr. 6, D-79104
Freiburg, Germany*

²*Institute of Theoretical Astrophysics, University of Oslo, P.O. Box
1029 Blindern, N-0315 Oslo, Norway*

Abstract. It is widely believed that the heating of the chromosphere in quiet-Sun internetwork regions is provided by dissipation of acoustic waves that are excited by the convective motions close to the top of the convection zone and in the photospheric overshoot layer. This view lately became challenged by observations suggesting that the acoustic energy flux into the chromosphere is too low, by a factor of at least ten. Based on a comparison of TRACE data with synthetic image sequences for a three-dimensional simulation extending from the top layers of the convection zone to the middle chromosphere, we come to the contradicting conclusion that the acoustic flux in the model provides sufficient energy for heating the solar chromosphere of internetwork regions. The role of a weak magnetic field and associated electric current sheets is also discussed.

1. Introduction

In two recent papers Fossum & Carlsson (2005, 2006, hereafter FC05 and FC06) come to the conclusion that ‘high-frequency acoustic waves are not sufficient to heat the solar chromosphere’. This conclusion is based on a study of image sequences from the 1600 Å channel of TRACE (*Transition Region and Coronal Explorer*). The continuum intensity at the wavelength of 160 nm originates from the upper photosphere. There, acoustic waves suffer no longer strong radiative damping and have not yet become strongly non-linear. Hence, the TRACE images seem to be an excellent means for measuring the total mechanical flux entering the chromosphere at its base. However, the mechanical flux cannot be measured directly but must be inferred from the measured intensity fluctuation $(\Delta I/I)_{160\text{ nm}}$. FC05 do this by comparing the average spectral power density for $(\Delta I/I)_{160\text{ nm}}^{\text{obs}}$ with those for corresponding synthetic intensity fluctuations $(\Delta I/I)_{160\text{ nm}}^{\text{synth}}$ from simulations with the one-dimensional radiation hydrodynamics code RADYN (e.g., Carlsson & Stein 1997). They find that the power spectra fit best for simulation runs that yield a mechanical flux at a height of 400 km (integrated over 5 to 50 mHz) of merely 438 W m^{-2} — ten times less than is needed to compensate the radiative losses of approximately 4300 W m^{-2} (excluding Lyman α) in the semi-empirical model of the chromosphere by Vernazza et al. (1981, hereafter VAL).

Here, we present new calculations based on the three-dimensional radiation hydrodynamic simulation by Wedemeyer et al. (2004, hereafter W04), which ex-

hibit a dynamic pattern on a spatial scale too small to be resolved with TRACE. We discuss potential implications for the heating of the solar chromosphere.

2. Acoustic heating on small spatial scales

2.1. Three-dimensional non-magnetic simulations

The three-dimensional radiation hydrodynamics simulations by W04 were carried out with the computer code CO⁵BOLD (Freytag et al. 2002) and cover a horizontal region of $7''7 \times 7''7$ and extend from the upper convection zone at a depth of 1400 km to the middle chromosphere at a height of 1710 km. The spatial resolution is 40 km in the horizontal directions and 12 km vertically in the atmosphere. Magnetic fields are not included so that this model represents very quiet internetwork regions only.

In order to keep the computations feasible, the radiative transfer is treated grey (i.e. frequency-independent) and under the assumption of local thermodynamic equilibrium (LTE). These are severe assumptions for the upper photosphere and the chromosphere above but are reasonable for the low photosphere in the framework of time-dependent three-dimensional simulations. The model chromosphere is – in sharp contrast to semi-empirical static models like, e.g., those by VAL – highly intermittent in time and space, consisting of a dynamic mesh-work like pattern of hot shock wave fronts and cool post-shock regions in between. The assumptions made for the radiative transfer affect the temperature amplitudes and the chromospheric energy balance but are reasonable for the low photosphere, where the acoustic waves are excited. The model provides sufficient acoustic energy to counterbalance the radiative losses in the internetwork chromosphere without need for further contributions from processes related to magnetic fields (Wedemeyer 2003).

2.2. Intensity synthesis

The general procedure for our analysis can be summarised like this: (i) Synthesis of the continuum intensity at relevant ultra-violet (UV) wavelengths, (ii) integration of the intensity over wavelength to a synthetic TRACE channel, (iii) image degradation to the spatial resolution due to the instrument's optics, (iv) spatial intensity integration for mimicking the TRACE detector (pixels), and finally (v) calculation of (average) power spectra from the intensity sequences resulting from step (i) to (iv).

We use a short simulation sequence from W04 with a duration of 10 min and a cadence of 10 s. For each snapshot we calculate continuum intensity maps with the radiative transfer code Linfor3D (<http://www.aip.de/~msteffen/>) at wavelengths from 150 nm to 180 nm with an increment of 5 nm, covering the wavelength range relevant for the TRACE 160 nm channel. With increasing wavelength the intensity fluctuations become smaller, whereas the absolute intensity level grows strongly. Including longer wavelengths thus effectively reduces the signal $I / \langle I \rangle$ and the resulting spectral power density. The intensity sequences for different wavelengths (150 nm - 180 nm) are now integrated according to the instrument's transmission curve (Handy et al. 1999, see also

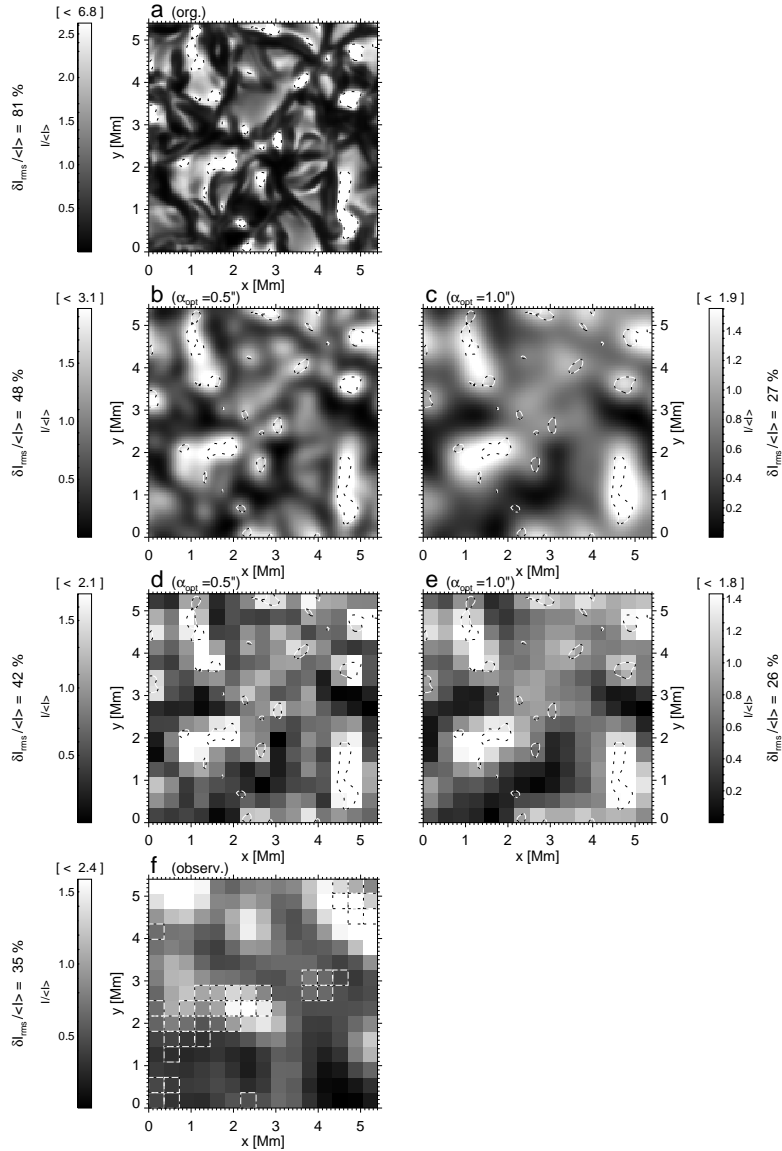


Figure 1. Synthetic intensity images for 160 nm passband of TRACE: **a)** original image, **b)** degraded to a spatial resolution of $0''.5$, and **d)** after integration on TRACE $0''.5$ pixels. The image degradation is repeated for a coarser resolution of $1''.0$ in panel **c)** but with the same pixel size in panel **e)**. The dashed contours for the original intensity in panel **a)** help to identify the enclosed regions in the other panels. Panel **f)** shows observed TRACE data from September 28th, 2005, taken from a data set kindly provided by Fossum & Carlsson. The dashed squares mark pixels that would be disregarded according to the pixel selection method by FC06. The grey scale ranges of the panels are clipped individually. The maximum value is given in brackets above each legend. The intensity contrast is noted on the side of each panel.

<http://www.lmsal.com/solarsoft>), resulting in a short sequence for the synthetic TRACE channel. A typical intensity image is shown in Fig. 1a.

In the next step the synthetic intensity images are convolved with a point-spread function (PSF) in order to mimic the instrument's UV optics (Fig. 1b). Unfortunately, the PSF of TRACE is poorly known but might be represented best by a Gaussian kernel of width (FWHM) larger than $0''.5$ but not more than $1''$ (Krijger et al. 2001; Schneider et al. 2004; Schrijver 2006). The detector of TRACE has a pixel-scale of $0.5''/\text{px}$. A synthetic pixel thus corresponds to spatial integration over (square) regions of 9×9 model grid cells (Fig. 1c). Note that FC05 additionally apply a binning of 2×2 pixels but FC06 use no binning. An example of observational data from FC06 is shown in Fig. 1d for comparison.

Figure 1 clearly demonstrates that the pattern on small spatial scales is lost and only the brightest features are still visible in the synthetic image. Consequently the intensity contrast decreases from 81 % to 42 % for the displayed snapshot (89 % and 33 %, respectively, for the whole sequence). The lower intensity contrast of the observational data (35 % for the displayed region, 30 % for the whole time series for that region, and 26 % for the time series of all pixels according to the mask by FC06) suggests that the true resolution of TRACE might be coarser than the $0''.5$ shown in Fig. 1c, which represents a lower limit only. A resolution of $1''$, on the other hand, might indeed be considered an upper limit as it reduces the contrast of the synthetic images to 33 % for the displayed snapshot and only 26 % for the whole time series.

2.3. Spectral power density

We derive the temporal spectral power density (one-sided) for each spatial position in the synthetic image sequences separately. The horizontally averaged power spectra are shown in Fig. 2 for the sequence with the original spatial resolution of the input model and also for the two sequences degraded to lower resolution ($0''.5$ and $1''$). For comparison we plot the power spectra that we calculate from the observed TRACE sequence from September 28th, 2005 (FC05), (i) for the pixel sample of FC06 and (ii) for the small region shown in Fig. 1d. Image degradation obviously suppresses power on small spatial scales. The average power is reduced by a factor of 10 at 12 mHz for the degraded sequence with a resolution of $0''.5$, with respect to the original image sequence, whereas a resolution of $1''$ results in a factor of 27 for the same frequency (see Fig. 2). The reduction in power increases with frequency up to ~ 20 mHz as higher frequencies are connected to smaller wavelengths (of acoustic waves) that are more severely affected by a limited resolution than large-scale fluctuations. The power when using a PSF of $1''$ width agrees well with the observational results in the range 3 mHz to ~ 12 mHz.

The discrepancy at low frequencies is due to the short sequence duration, which results in a frequency resolution (see solid circles) that is too small to resolve the local minimum at $\nu \approx 2.5$ mHz. A longer synthetic image sequence at 160 nm with a duration of 76 min and a cadence of 30 s, that we calculated in addition, shows results similar to those for the short sequence at 160 nm with respect to absolute magnitude of power and the relative effect of degrading the spatial resolution. The longer duration provides much finer frequency sampling

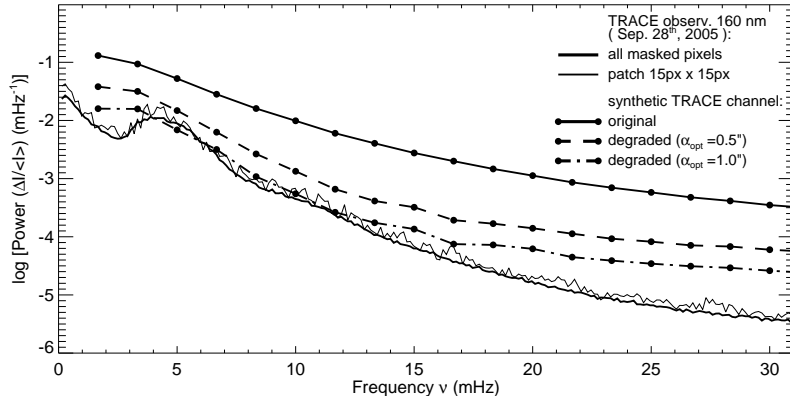


Figure 2. Average one-sided power density spectra for the short sequence of synthetic TRACE images (lines with dots) for original spatial resolution (solid), degradation to $0''.5$ (dashed) and $1''$ (dot-dashed) without pixel-binning. The solid dots mark the data points. The two other curves are calculated from observational data from September 28th, 2005, in the same way as done for the synthetic sequences. The thick curve includes all pixels according to the mask by FC06, whereas the thin one is for the region displayed in Fig. 1d only.

so that the average power spectrum indeed exhibits a local minimum at low frequencies.

The increasing difference at higher frequencies is most likely connected to the assumption of LTE that had to be made in order to keep the calculations computationally tractable. The assumption is validated by comparison with a more detailed calculation with the RH code (see, e.g., Uitenbroek 2000) for eight 2D slices from the model for a wavelength of 160 nm, taking into account deviations from LTE. The rms fluctuations of the resulting intensity samples are 150.8 % for Linfor3D (LTE), 199.3 % for RH in LTE, and 134.9 % for RH in NLTE. The difference for the LTE samples must be attributed to (i) the assumption of 2D for our application of RH in contrast to full 3D with Linfor3D, (ii) differences in opacity data (in particular concerning photoionisation cross-sections of silicon), and (iii) the neglect of continuum scattering in Linfor3D. The latter, however, is expected to be of minor importance as there are few continuum scattering processes that are relevant at wavelengths around 160 nm. More important is the correct treatment of bound-free transitions of silicon (taken into account in RH). They can be regarded as bound-free "two-level" resonance scatterers and effectively smooth out fluctuations. Nevertheless this qualitative comparison demonstrates that neglecting non-LTE effects tends to produce too large relative intensity fluctuations and with that an excess in average power for higher frequencies as visible in Fig. 2.

In addition, a simulation sequence with non-grey radiative transfer (Wedemeyer 2003) was used for intensity synthesis at 160 nm. The resulting power spectra at original and lowered resolution are very similar to the grey sequence used here.

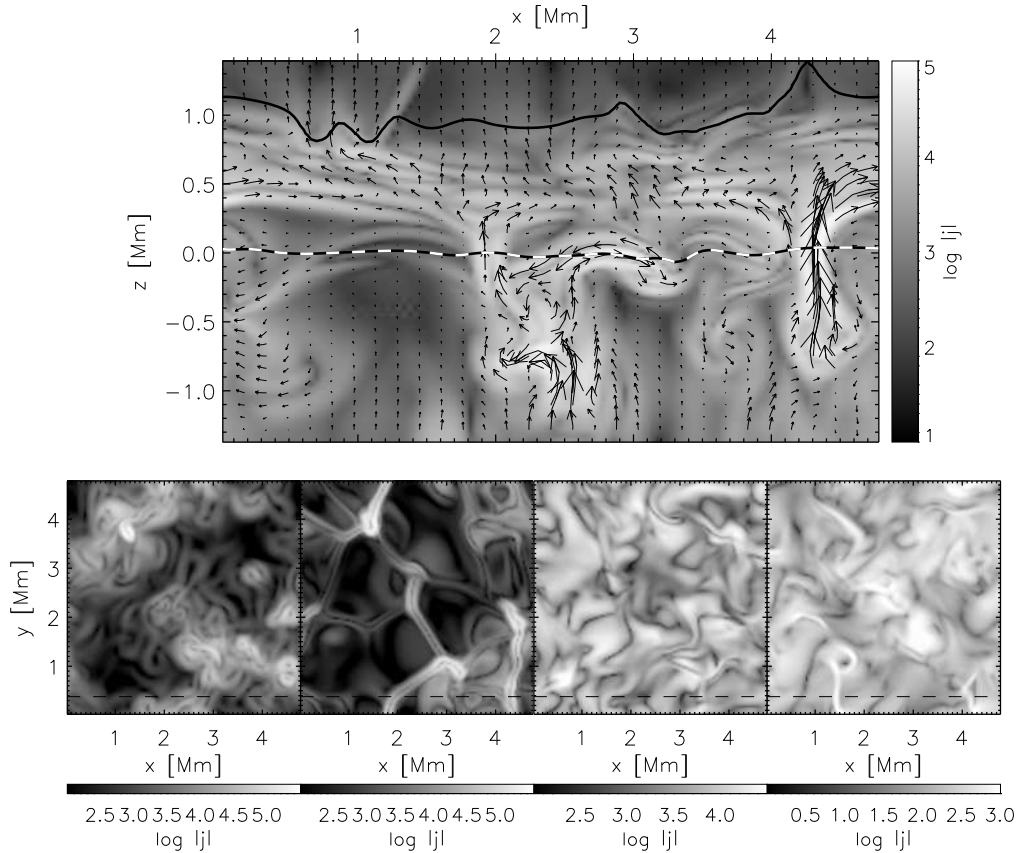


Figure 3. Logarithmic current density, $\log |j|$, in a vertical cross section (top panel) and in four horizontal cross sections in a depth of 1180 km below, and at heights of 90 km, 610 km, and 1310 km above the mean surface of optical depth unity from left to right, respectively. The arrows in the top panel indicate the magnetic field strength and direction. The dashed line indicates the position of the vertical section. $[j] = 3 \cdot 10^5 \text{ A/m}^2$.

3. Ohmic dissipation of chromospheric current sheets

3.1. Three-dimensional MHD simulation

We have also carried out a three-dimensional simulation including magnetic fields. The computational domain extends from a depth of 1400 km below the mean surface of optical depth unity to 1400 km above it well into the chromospheric layers. The horizontal extent is only slightly smaller than for the model by W04. See Schaffenberger et al. (2005, 2006) for details.

The MHD simulation starts with a homogeneous, vertical, unipolar magnetic field of a flux density of 10 G superposed on a previously computed, relaxed model of thermal convection. This flux density is thought to represent magnetoconvection in a very quiet network-cell interior. The magnetic field is constrained to have vanishing horizontal components at the top and bottom boundary but lines of force can freely move in the horizontal direction. Because the top bound-

ary is located in the chromosphere, the magnetic field can freely expand with height through the photospheric layers into the more or less homogeneous chromospheric field, different from conventional simulations that extend to a height of typically 600 km only.

A very common phenomenon in this simulation is the formation of a ‘magnetic canopy field’ that extends in a more or less horizontal direction over expanding granules and between photospheric flux concentrations. The formation of such canopy fields proceeds by the action of the expanding flow above granule centres. This flow transports ‘shells’ of horizontal magnetic field to the upper photosphere and lower chromosphere, where shells of different field directions may be pushed close together, leading to a complicated network of current sheets in a height range from approximately 400 to 900 km.

This network can be seen in Fig. 3 (top), which shows, for a typical snapshot of the simulation, the logarithmic current density, $\log |j|$, together with arrows indicating the magnetic field strength and direction. Figure 3 (bottom) shows from left to right $\log |j|$ in four horizontal cross sections in a depth of 1180 km below, and at heights of 90 km, 610 km, and 1310 km above the mean surface of optical depth unity. Higher up in the chromosphere (rightmost panel), thin current sheets form along shock fronts, e.g., in the lower left corner near $x = 1.4$ Mm.

3.2. Ohmic dissipation

In this simulation we have not taken an explicit magnetic diffusion into account so that the effective electrical conductivity is determined by the inherent artificial diffusion of the numerical scheme. Therefore, due to lack of a realistic electric conductivity, we here use molecular values when computing the ohmic dissipation of the chromospheric current sheets. Although the values might be orders of magnitude too high, they still can be employed for the following calculation, which gives a rough idea about the significance of ohmic dissipation for chromospheric heating. The typical current density in the height range from 400 to 900 km of Fig. 3 (top) is $j = 0.03 \text{ A m}^{-2}$. The electrical conductivity, σ , in the photosphere and the lower chromosphere is about 10 to 100 A/Vm (Stix 2002). Using this value, the ohmic dissipation is

$$P_j = \frac{1}{\sigma} j^2 \approx \frac{1}{10 \dots 100} 0.03^2 \approx 10^{-5} \dots 10^{-4} \text{ W m}^{-3}. \quad (1)$$

When integrating over a height range of 500 km this heat deposition leads to an energy flux of 5 to 50 W m^{-2} . This value is about two orders of magnitude short of being relevant for chromospheric heating. However, the amplitude and width of the current sheets in the simulation is determined by the spatial resolution of the computational grid rather than by the molecular conductivity. The effective conductivity in the simulation may easily be two orders of magnitude lower so that magnetic heating by ohmic dissipation must be seriously taken into account as a chromospheric heating agent. Further simulations, taking explicit ohmic diffusion into account will clarify this issue.

4. Discussion

The photosphere of the model by W04 can account for many aspects of observations of internetwork regions (see, e.g., Leenaarts & Wedemeyer-Böhm 2005). Here we provide evidence that the UV intensity in the TRACE 160 nm channel is matched reasonably well, too. When degraded to the spatial resolution of the instrument, the synthetic intensity images presented here have similar contrasts and also result in average spectral power densities similar to the TRACE observations. The power spectra exhibit an enhancement around periods of 5 min and otherwise a decrease with frequency as it was found by FC05 and FC06 both from observations and their 1D simulations.

At higher frequencies, however, we derive too much power from the synthetic image series. This discrepancy is most likely due to the LTE assumption made for the intensity synthesis with Linfor3D. The test calculations with the RH code show that taking into account deviations from LTE reduces the intensity contrast by $\sim 60\%$ compared to the LTE case for a wavelength of 160 nm. The deviation from LTE at the shorter wavelengths is mostly due to the strong over-ionisation of Si I, which affects the continuum forming bound-free transitions. Similar to true continuum scattering, this effect smoothes out fluctuations, so that the LTE assumption used here actually tends to produce too large fluctuations and thus an excess in power. We argue that the derived reduction of $\sim 60\%$ in intensity contrast can be considered as an upper limit for the influence of this scattering-like process. In contrast, the deviations from LTE are much smaller for the longer wavelengths. For a rough estimate we derive an average ratio of LTE and NLTE intensities based on the RH calculations and use it to scale the LTE intensities of the whole synthetic 160 nm sequence. This “pseudo-NLTE” time series leads to a further reduction in power by approximately a factor of two around periods close to 5 min to four for higher frequencies. The tendency of larger power reduction with increasing frequency might be even more enhanced by non-LTE effects being more important on time scales too short for relaxation to equilibrium conditions. The “pseudo-NLTE” estimate is of course an order of magnitude approximation only and needs to be replaced with detailed NLTE calculations that include not only 160 nm but the whole wavelength range relevant for the TRACE channel. Taking into account line blanketing acts in the opposite direction by reducing the intensity at the longer wavelengths and thus increasing the relative fluctuations. A comparison of the spectra calculated with MULTI for the VAL model A results in a reduction of integrated intensity by a factor of ~ 2 (Carlsson 2006). But whether it really counterbalances the expected NLTE effects and if so by how much and for which frequencies remains subject to detailed radiative transfer calculations.

The computational box of the hydrodynamical simulation is small ($5.6 \text{ Mm} \times 5.6 \text{ Mm}$). Consequently, the number of possible oscillation modes is much smaller than in the real Sun so that the power in the model is distributed over a smaller number of modes. The total energy content of the modes, however, remains the same. Also the finite grid resolution limits the treatment of high-frequency waves but FC06 state that the neglect of frequency beyond 20 mHz is not an important omission.

When computing the mechanical energy flux from the intensity fluctuations, FC05 and FC06 assume that the resolution of TRACE is sufficient to fully cap-

ture the energy carrying waves. FC06 state that tests with 2D models related to the hydrodynamic simulations by Hansteen (2004) imply that only a factor of two in acoustic flux is missed due to insufficient spatial resolution. In contrast our 3D study presented here shows that the unresolved small-scale pattern provides more power by an order of magnitude or even more.

At this stage we cannot exactly determine how much of the additional power hidden on small spatial scales is indeed transported to the chromosphere and how much remains in the photosphere and therefore does not contribute to chromospheric heating. Separating the acoustic flux from the total mechanical flux is not easy for our 3D model the latter gets on average even negative in the middle photosphere as a consequence of convective overshooting. There is a local maximum of the radiative flux divergence in the low chromosphere and a mechanical counterpart of opposite sign that we interpret as evidence for the conversion of mechanical energy provided by acoustic waves into thermal energy, which is subsequently emitted in form of radiation (Wedemeyer 2003). Integration of the mechanical flux divergence over the height range from 570 km to 1710 km results in an acoustic energy flux of 7.9 kW m^{-2} which is sufficient to counterbalance the (semi-)empirically determined radiative energy losses from the chromosphere (see, e.g, VAL). Moreover, the total mechanical flux at a height of 800 km (which approaches the pure acoustic flux there) amounts to 3.8 kW m^{-2} and is thus in line with the 1D models by Rammacher (2005).

On the other hand, the energy flux due to Ohmic dissipation of current sheets in the MHD model chromosphere is only of the order of 5 to 50 W m^{-2} . This value must be considered as a lower limit only because of the uncertainty in the electrical conductivity. It can thus not be ruled out that the magnetic heating contribution might be underestimated by even two orders of magnitude.

Although the energy balance of the model chromosphere is affected by a too simple treatment of the radiative transfer, the calculations presented here suggest that the acoustic contribution to chromospheric heating cannot be neglected. Magnetic fields may also play an indirect role for guiding acoustic waves and for mode conversion (Suematsu 1990; Ulmschneider et al. 1991; Jefferies et al. 2006).

5. Conclusions

Based on the analysis presented here we conclude that TRACE might miss acoustic power by at least one order of magnitude due to its limited spatial resolution. Horizontal flows, as they are clearly seen within the reversed granulation pattern, contribute to the intensity variations although their relevance for the energy transport to the upper layers is not clear yet.

Matching the empirical power spectra with a model that has enough acoustic power to counterbalance the observed chromospheric emission should not be interpreted such that high-frequency waves alone are sufficient to heat the chromosphere. It is not clear from this study how important the small relative power contribution of high-frequency waves is for chromospheric heating. Moreover, the model used here exhibits a chromosphere with pronounced dynamics and a highly inhomogeneous structure – in sharp contrast to static and one-dimensional semi-empirical VAL-like models. The ubiquitous shock waves,

which produce our model chromosphere's characteristic structure, play certainly an important role for the energy balance of our model chromosphere.

It must be emphasised that – owing to simplifications that are necessary in order to keep the problem computationally tractable – the topic should be addressed again with detailed NLTE calculations. Nevertheless, the presented study clearly demonstrates that three-dimensional radiation hydrodynamics simulations in principle can reproduce the TRACE observations of internetwork regions without strong need for magnetic fields, although weak fields are most likely an integral part of those regions. We conclude that an acoustic “basal flux” (Schrijver 1987) must still be considered a possible option for heating the chromosphere of internetwork regions.

Acknowledgments. We thank the CSPM organisers for a very good meeting and M. Carlsson, K. Muglach, C. Schrijver, R. Rutten, and H. Uitenbroek for discussion and helpful comments. We are grateful to A. Fossum for kindly providing observational data and useful remarks regarding data reduction. Thanks go also to M. Steffen, H.-G. Ludwig, and B. Freytag for their support for Linfor3D and CO⁵BOLD. H. Uitenbroek friendly provided his RH code. This work was supported by the *Deutsche Forschungsgemeinschaft (DFG)*, grant Ste 615/5.

References

- Carlsson M., Stein R. F., 1997, ApJ481, 500
 Carlsson, M. 2006, priv. comm.
 Fossum, A. & Carlsson, M. 2005, Nat, 435, 919 (FC05)
 Fossum, A. & Carlsson, M. 2006, ApJ, 646, 579 (FC06)
 Freytag, B., Steffen, M., & Dorch, B. 2002, Astron. Nachr., 323, 213
 Handy, B. N., Acton, L. W., Kankelborg, C. C., et al. 1999, Solar Phys., 187, 229
 Hansteen, V. H. 2004, in IAU Symposium, ed. A. V. Stepanov, E. E. Benevolenskaya, & A. G. Kosovichev, 385
 Jefferies, S. M., McIntosh, S. W., Armstrong, J. D., et al. 2006, ApJ, 648, L151
 Krijger, J. M., Rutten, R. J., Lites, B. W., et al. 2001, A&A, 379, 1052
 Leenaarts, J. & Wedemeyer-Böhm, S. 2005, A&A, 431, 687
 Rammacher, W. 2005, in ESA SP-596: Chromospheric and Coronal Magnetic Fields, ed. D. E. Innes, A. Lagg, & S. A. Solanki
 Schaffenberger, W., Wedemeyer-Böhm, S., Steiner, O., & Freytag, B. 2005, in Chromospheric and Coronal Magnetic Fields, D. Innes, A. Lagg, S. Solanki, & D. Danesy (eds.), ESA Publication SP-596, (CD-ROM) p. 65.1
 Schaffenberger, W., Wedemeyer-Böhm, S., Steiner, O., & Freytag, B. 2006, in Solar MHD Theory and Observation: A High Apatial Resolution Perspective, H. Uitenbroek, J. Leibacher, & R.F. Stein (eds.), ASP Conference Series 354, p. 351-356
 Schneider, G., Pasachoff, J. M., & Golub, L. 2004, Icarus, 168, 249
 Schrijver, C. J. 1987, A&A, 172, 111
 Schrijver, C. J. 2006, priv. comm.
 Stix, M. 2002, The Sun, 2nd edition, Springer
 Suematsu, Y. 1990, in LNP Vol. 367: Progress of Seismology of the Sun and Stars, ed. Y. Osaki & H. Shibahashi, 211
 Uitenbroek, H. 2000, ApJ, 536, 481
 Ulmschneider, P., Zaehring, K., & Musielak, Z. E. 1991, A&A, 241, 625
 Vernazza, J. E., Avrett, E. H., & Loeser, R. 1981, ApJS, 45, 635 (VAL)
 Wedemeyer, S. 2003, PhD thesis, University of Kiel, <http://e-diss.uni-kiel.de/diss.764/>
 Wedemeyer, S., Freytag, B., Steffen, M., Ludwig, H.-G., & Holweger, H. 2004, A&A, 414, 1121 (W04)